

Optically Pumped Cs Magnetometers Enabling a High-Sensitivity Search for the Neutron Electric Dipole Moment

C. Abel,¹ S. Afach,^{2,3} N. J. Ayres,^{1,3} G. Ban,⁴ G. Bison,^{2,*} K. Bodek,⁵ V. Bondar,^{2,3,6} E. Chanel,⁷ P.-J. Chiu,^{2,3} C. B. Crawford,⁸ Z. Chowdhuri,² M. Daum,² S. Emmenegger,³ L. Ferraris-Bouchez,⁹ M. Fertl,^{2,3,10} B. Franke,^{2,3,†} W. C. Griffith,¹ Z. D. Grujić,^{11,12} L. Hayen,⁶ V. H elaine,^{2,4} N. Hild,^{2,3} M. Kasprzak,^{2,6,11,‡} Y. Kermaidic,^{9,§} K. Kirch,^{2,3} P. Knowles,^{11,¶} H.-C. Koch,^{2,10,11} S. Komposch,^{2,3} P. A. Koss,⁶ A. Kozela,¹³ J. Krempel,³ B. Lauss,² T. Lefort,⁴ Y. Lemi ere,⁴ A. Leredde,⁹ A. Mtchedlishvili,² P. Mohanmurthy,^{2,3} M. Musgrave,^{1,**} O. Naviliat-Cuncic,⁴ D. Pais,^{2,3} A. Pazgalev,¹⁴ F. M. Piegsa,⁷ E. Pierre,^{2,4} G. Pignol,⁹ P. N. Prashanth,^{2,6} G. Qu em ener,⁴ M. Rawlik,³ D. Rebreyend,⁹ D. Ries,¹⁵ S. Roccia,^{16,17} D. Rozpedzik,⁵ P. Schmidt-Wellenburg,² A. Schnabel,¹⁸ N. Severijs,⁶ R. Tavakoli Dinani,⁶ J. Thorne,^{1,7} A. Weis,¹¹ E. Wursten,^{6,††} G. Wyszynski,^{3,5} J. Zejma,⁵ and G. Zsigmond²

¹*Department of Physics and Astronomy, University of Sussex, BN1 9QH Brighton, England, United Kingdom*

²*Paul Scherrer Institute, 5232 Villigen, Switzerland*

³*Eidgen ossische Technische Hochschule Z urich, Institute for Particle Physics and Astrophysics, 8093 Z urich, Switzerland*

⁴*Normandie Universit e, ENSICAEN, UNICAEN,*

Centre National de la Recherche Scientifique IN2P3, LPC Caen, Caen, France

⁵*Marian Smoluchowski Institute of Physics, Jagiellonian University, 30-348 Cracow, Poland*

⁶*Instituut voor Kern- en Stralingsfysica, Katholieke Universiteit Leuven, 3001 Leuven, Belgium*

⁷*Laboratory for High Energy Physics, Albert Einstein Center for Fundamental Physics, University of Bern, 3012 Bern, Switzerland*

⁸*University of Kentucky, Lexington, Kentucky 40506, USA*

⁹*Universit e Grenoble Alpes, Centre National de la Recherche Scientifique, Grenoble INP, LPSC-IN2P3, Grenoble, France*

¹⁰*Institute of Physics, Johannes Gutenberg University Mainz, 55128 Mainz, Germany*

¹¹*Physics Department, University of Fribourg, 1700 Fribourg, Switzerland*

¹²*Institute of Physics Belgrade, University of Belgrade, 11080 Belgrade, Serbia*

¹³*Henryk Niewodniczanski Institute of Nuclear Physics, Polish Academy of Sciences, 31-342 Cracow, Poland*

¹⁴*Ioffe Physical Technical Institute, 194021 Saint Petersburg, Russia*

¹⁵*Institut f ur Kernchemie, Johannes Gutenberg University Mainz, 55128 Mainz, Germany*

¹⁶*CSNSM, Universit e Paris Sud, Centre National de la Recherche Scientifique IN2P3, Universit e Paris Saclay, Orsay, France*

¹⁷*Institut Laue-Langevin, 38042 Grenoble, France*

¹⁸*Physikalisch Technische Bundesanstalt, D-10587 Berlin, Germany*

(Dated: May 17, 2022)

An array of sixteen laser-pumped scalar Cs magnetometers was part of the neutron electric dipole moment (nEDM) experiment taking data at the Paul Scherrer Institute in 2015 and 2016. It was deployed to measure the gradients of the experiment’s magnetic field and to monitor their temporal evolution. The originality of the array lies in its compact design, in which a single near-infrared diode laser drives all magnetometers that are located in a high-vacuum chamber, with a selection of the sensors mounted on a high-voltage electrode. We describe details of the Cs sensors’ construction and modes of operation, emphasizing the accuracy and sensitivity of the magnetic field readout. We present two applications of the magnetometer array directly beneficial to the nEDM experiment: (i) the implementation of a strategy to correct for the drift of the vertical magnetic field gradient and (ii) a procedure to homogenize the magnetic field. The first reduces the uncertainty of the new nEDM result. The second enables transverse neutron spin relaxation times exceeding 1500 s, improving the statistical sensitivity of the nEDM experiment by about 35% and effectively increasing the rate of nEDM data taking by a factor of 1.8.

I. INTRODUCTION

The experimental search for a permanent electric dipole moment of the neutron (nEDM) has been an important topic of fundamental research since the early 1950s [1, 2]. Over the years, the experimental sensitivity has improved by more than six orders of magnitude, with a significant contribution coming from the development of ultracold neutron (UCN) sources [3], allowing the storage of neutrons in a “bottle” for hundreds of seconds. The experimental method applied to search for an nEDM with ultracold neutrons is based on a precise determina-

* corresponding author: georg.bison@psi.ch

† present address: TRIUMF, Vancouver, Canada

‡ corresponding author: malgorzata.kasprzak@psi.ch

§ present address: Max Planck Institut f ur Kernphysik, Heidelberg, Germany

¶ present address: LogrusData, Toronto, Ontario, Canada

** present address: Massachusetts Institute of Technology, Cambridge, MA, USA

†† corresponding author: elise.wursten@cern.ch; present address: CERN, Geneva, Switzerland

tion of the neutron spin precession frequency in static homogeneous parallel/antiparallel magnetic and electric fields by the Ramsey technique of (time-)separated oscillatory fields [4]. The statistical and systematic uncertainties of this method are strongly dependent on the (non)uniformity of the magnetic field \mathbf{B} in which the neutrons precess.

This article is the second episode in a trilogy of papers that comprehensively treat the uncertainties in nEDM searches that originate from the inhomogeneity of the magnetic field. The first episode [5] gives a general introduction to the subject, defines the way we characterize gradients, and derives the relevant criteria for nEDM experiments. In the second episode – this paper – we discuss in detail the approach used to measure and compensate magnetic field gradients in the 2015 and 2016 data runs of the nEDM experiment at the Paul Scherrer Institute (PSI). The third part will present the off-line characterization of the magnetic field uniformity in the apparatus with an automated field-mapping device.

The nEDM apparatus at PSI is an upgraded version of the Sussex–RAL–ILL apparatus [7] that is equipped with two high-sensitivity systems for monitoring magnetic field changes, namely a ^{199}Hg co-magnetometer [6, 7] and an array of sixteen laser-pumped Cs magnetometers [8, 9]. The PSI-nEDM experiment was the first that used simultaneously a co-magnetometer and an array of external magnetometers during data taking. The Hg co-magnetometer employs an ensemble of spin-polarized ^{199}Hg atoms which occupy the same storage volume as the UCN, and whose spin precession frequency is used to correct for drifts of the magnetic field in every Ramsey cycle. The array of Cs magnetometers located above and below the storage chamber measures the spatial distribution of the magnetic field, allowing for control of the field homogeneity and extraction of the gradients across the neutron storage chamber. The focus of this article is the implementation and application of the Cs magnetometer array. In Section II we describe the principle of the PSI-nEDM measurement with emphasis on the required magnetic field sensitivity and resolution of the magnetic field gradient. Section III provides a technical description of the Cs magnetometer array, including the design of the Cs magnetometers, their modes of operation and their performance in terms of magnetic field sensitivity and accuracy. Section IV details the applications of the Cs magnetometer array in the nEDM experiment. A description of how to extract magnetic field gradients from the array field measurements is provided in Section IV A and Section IV B presents the procedure used to optimize the magnetic field.

II. THE NEDM EXPERIMENT AT PSI

Figure 1 shows the general scheme of the PSI-nEDM experiment [10], further called the ‘nEDM experiment’. The cylindrical neutron storage chamber – that also

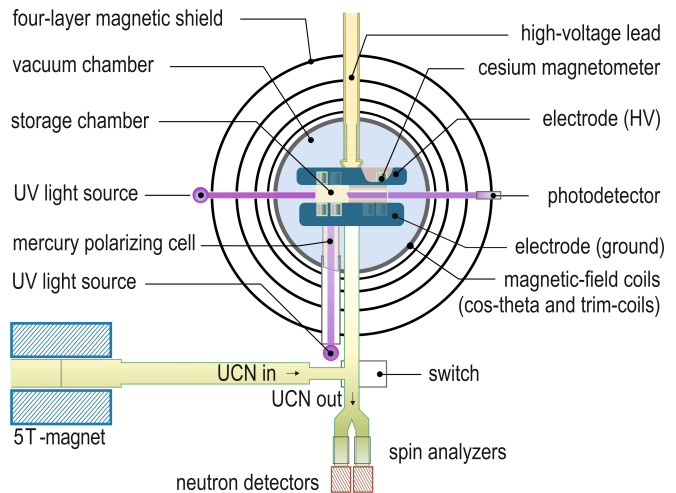


FIG. 1. Scheme of the nEDM apparatus.

contains the ^{199}Hg co-magnetometer – consists of a polystyrene ring coated with deuterated polystyrene [11] and aluminum end caps coated with diamond-like carbon [12]. The latter serve as high-voltage and ground electrodes, which can generate a vertical electric field of up to 15 kV/cm in the chamber. The height of the cylinder – i.e., the distance between the electrodes – is 120 mm, and the radius is 235 mm. The Cs magnetometers that measure the magnetic field gradients are mounted on the high voltage and ground electrodes. The storage chamber is located inside an aluminum vacuum chamber, onto which a cos-theta coil is wound together with a set of 30 trim-coils. The cos-theta coil produces a vertical, static magnetic field of $\approx 1 \mu\text{T}$, while the set of trim-coils are used to homogenize the field and to apply specific field gradients when necessary. The vacuum chamber is surrounded by a 4-layer μ -metal shield. The whole setup is enclosed in an air-conditioned, temperature-stabilized wooden hut. Three pairs of large ($\approx 8\text{m} \times 6\text{m}$) rectangular coils are mounted outside the hut and dynamically compensate the outer ambient field [13].

The operation of the apparatus during data taking with UCN was recently reviewed in [14]. The effect of a finite nEDM, d_n , when the neutron is exposed to both an electric field \mathbf{E} and a magnetic field \mathbf{B} is an electric-field-dependent shift of the neutron spin precession frequency. Statistical uncertainties in the determination of that frequency by Ramsey’s method [4] propagate to the sensitivity of the nEDM measurement

$$\sigma(d_n) \geq \frac{\hbar}{2\alpha T E \sqrt{N} \sqrt{N_{\text{cycles}}}}, \quad (1)$$

where α is the contrast of the Ramsey fringe, T is the precession time, E the electric field strength, N the number of detected neutrons in one Ramsey cycle, and N_{cycles} the number of such cycles. Details of this procedure are given in [15]. The contrast α is determined by the transverse neutron spin depolarization time, and can be

significantly improved by homogenizing the longitudinal (vertical) component of the magnetic field, as discussed in Section IV B.

The statistical sensitivity of the Sussex–RAL–ILL experiment [16, 17] – which led to the current best value for d_n [18] – was $\sigma_{\text{day}}(d_n) \approx 2 \times 10^{-25} e \cdot \text{cm}$ per day ($N_{\text{cycles}} = 400$). In the nEDM experiment at PSI this value was improved by increasing α (see Section IV B 4), E , and neutron counting statistics and was on average $\sigma_{\text{day}}(d_n) \approx 1.1 \times 10^{-25} e \cdot \text{cm}$ per day ($N_{\text{cycles}} = 288$).

In order to keep the systematic uncertainty related to the control of the magnetic field and its gradients below the statistical sensitivity in Eq. (1), the resolution of the magnetic field measurement in one Ramsey cycle should be:

$$\sigma(B) \ll \frac{E\sqrt{2N_{\text{cycles}}}\sigma_{\text{day}}(d_n)}{\mu_n}, \quad (2)$$

which gives $\sigma(B) \ll 0.5$ pT for the PSI-nEDM experiment. This resolution is provided by the ^{199}Hg co-magnetometer, whose spin precession frequency f_{Hg} is used to monitor and correct for changes of the magnetic field from one Ramsey cycle to the next [7]. The sensitivity of the ^{199}Hg co-magnetometer is on average better than 80 fT per Ramsey cycle, effectively reducing the contribution of magnetic field fluctuations to a few % of the total uncertainty.

However, the use of the ^{199}Hg co-magnetometer has an important drawback: because the ultracold neutrons have a much lower kinetic energy than the ^{199}Hg atoms, they average the magnetic field in the storage volume in a slightly different way. The ^{199}Hg atoms are a gas at room temperature and sample the volume uniformly, whereas the neutrons feel the pull of gravity and are more likely to be in the lower part of the precession chamber. As a consequence, the ratio $\mathcal{R} = f_n/f_{\text{Hg}}$ is affected by any vertical magnetic field gradient $\frac{\partial B_z}{\partial z}$ across the storage chamber. Adopting the notation of [5],

$$\mathcal{R} = \frac{f_n}{f_{\text{Hg}}} = \frac{\gamma_n}{\gamma_{\text{Hg}}} \left(1 + \frac{G_{\text{grav}}\langle z \rangle}{B_0} + \delta_{\text{other}} \right), \quad (3)$$

where γ_n and γ_{Hg} are the gyromagnetic ratios of the neutron and ^{199}Hg atom respectively, G_{grav} is a combination of the relevant vertical gradients (see Section IV A), $\langle z \rangle$ is the vertical displacement of the center of mass of the neutrons with respect to the center of the storage chamber, $B_0 = \langle B_z \rangle_{\text{Hg}}$ is the magnetic field averaged over the precession volume as measured by the ^{199}Hg co-magnetometer and δ_{other} encompasses all other effects that change the \mathcal{R} -ratio, such as, e.g., the motional false EDM [19] and the rotation of the Earth [20]. As the positive z -direction is defined upwards with respect to gravity, a negative value is expected for the average displacement $\langle z \rangle$ of the neutrons. The required resolution of the gradient measurements $\sigma(G_{\text{grav}})$ during one Ramsey cycle can be estimated in a similar way as $\sigma(B)$ leading

to

$$\sigma(G_{\text{grav}}) \ll \frac{\sigma(B)}{|\langle z \rangle|} \simeq 1.3 \text{ pT/cm}, \quad (4)$$

using $\langle z \rangle = -0.38(3)$ cm as determined in [5].

The temporal evolution of the magnetic field gradients was monitored with the array of sixteen Cs magnetometers installed close to the precession chamber. This allowed correcting for gradient drifts (Section IV A) and homogenizing the magnetic field using the variometer principle [21] (Sections III C and IV B). The latter resulted in larger values for the contrast α leading to a 35% increase in statistical sensitivity.

III. THE CS MAGNETOMETER ARRAY

This section describes the design, implementation and modes of operation of the Cs sensors installed above and below the precession chamber for monitoring magnetic field gradients.

A. Design and implementation

The magnetometer array consists of sixteen Cs sensors that are made of nonmagnetic materials and are vacuum-compatible. The compact design allows their mounting close to the storage chamber. The sixteen magnetometers are arranged in a three-layer gradiometer configuration with sensors located both above and below the storage chamber. Seven sensors are installed on the high voltage electrode, the centers of these sensors being 127.9(0.5) mm above the center plane of the neutron storage chamber. Nine sensors are installed below the ground electrode. They are arranged on two levels: 6 sensors are mounted on the aluminum plate directly below the ground electrode (128.5(0.5) mm below the center of the storage chamber), while three more sensors are positioned in a plane located 75(0.5) mm lower, as shown in Fig. 2. All sensors are placed with a lateral position accuracy of about 0.5 mm.

1. Principle of the Cs magnetometer

The main components of a Cs magnetometer are shown in Fig. 3. The actual field-sensing element of each sensor is an evacuated glass cell, with an inner diameter of ~ 28 mm, whose inner wall is coated by a thin layer of paraffin [23]. The Cs density in the cell is determined by the saturated vapor pressure of a metallic droplet of ^{133}Cs at room temperature. The droplet is contained in a sidearm connected to the main cell volume by a capillary. The cesium atoms are spin-polarized by optical pumping using circularly polarized laser light whose frequency is resonant with the $F_g=4 \rightarrow F_e=3$ hyperfine component

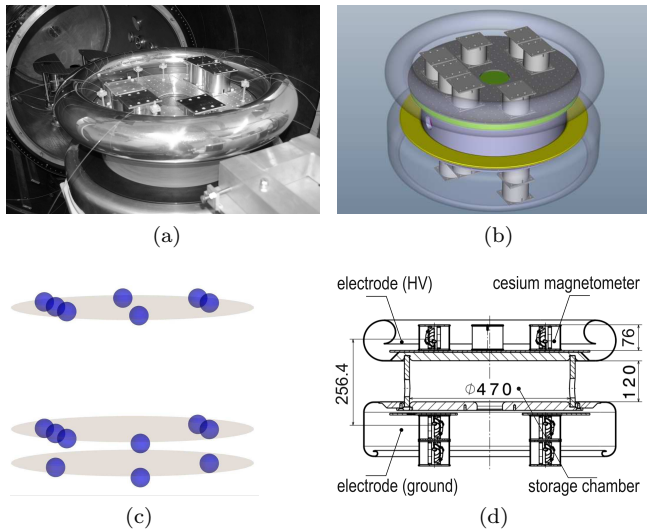


FIG. 2. Positions of the 16 Cs magnetometers in the nEDM experiment. Each sensor is enclosed in an aluminum cylinder which suppresses the interaction of its RF-field with the neighboring Cs sensors. (a) Storage chamber removed from the vacuum chamber (in the background) with 6 HV-compatible Cs magnetometers installed on an aluminum plate fixed to the HV electrode with corona ring. (b) Schematic view of the neutron storage chamber, the electrodes and the Cs magnetometers. (c) The blue spheres indicate the positions of the Cs sensors, they are arranged in three layers above and below the storage chamber. (d) Central vertical cut through (b) with dimensions in mm. The vertical distance of the Cs sensors from the center of the storage chamber is +127.9 mm, -128.5 mm, or -203.5 mm, the 13 closest magnetometers thus being a factor of 2.8 closer to the center of the precession chamber in comparison to the ^{87}Rb magnetometers in the earlier Sussex-RAL-ILL experiment [22].

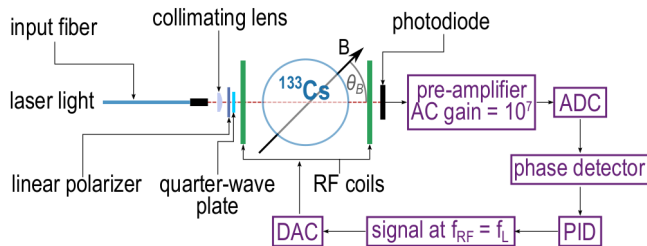


FIG. 3. Schematic of the Cs magnetometers' main components and electronics as described in the text.

of the D_1 transition. The laser beam traverses the cell at an angle of 45° with respect to the magnetic field \mathbf{B} . The light from a frequency-stabilized laser is delivered to the sensor by a $400\ \mu\text{m}$ multimode fiber. Before entering the cell, the light is collimated by a lens and circularly polarized by a linear polarizer and a quarter-wave plate (Fig. 3). The laser beam serves both to polarize the Cs atoms and to read out the precessing atomic spin polarization (optically detected magnetic resonance). When

exposed to the magnetic field \mathbf{B} , the magnetic moment associated with the spin polarization precesses at the Larmor frequency

$$f_L = \frac{\gamma_4}{2\pi} \|\mathbf{B}\|, \quad (5)$$

where $\gamma_4 \simeq 2\pi \times 3.50\ \text{Hz/nT}$ is the gyromagnetic ratio of the $F=4$ hyperfine level of the cesium ground state. The precession of Cs atoms imposes an oscillation on the transmission of the laser light, which is detected on the photodiode.

All 16 magnetometers are operated with light delivered by a single high-stability diode laser (Toptica, DL-pro 100) that is mounted in a dedicated housing in the temperature-stabilized room of the nEDM experiment. The laser frequency is actively locked to the $F_g=4 \rightarrow F_e=3$ hyperfine component of the Cs D_1 ($6S_{1/2} \rightarrow 6P_{1/2}$) transition at $\sim 895\ \text{nm}$ using Doppler-free saturation absorption spectroscopy (Toptica, CoSy), which allowed us to keep the laser continuously in frequency lock for weeks.

The beam from this laser is divided into multiple beams by a splitter system which is directly attached to the main vacuum chamber of the nEDM apparatus. The original beam is carried by a single $400\ \mu\text{m}$ multimode fiber to a beam homogenizer (SUSS MicroOptics) producing a flat-topped intensity profile of quadratic cross section. The homogenized beam is then imaged onto a bundle of 36 fibers with $400\ \mu\text{m}$ core diameter whose flat-polished input ends are arranged into a square brass-epoxy holder with an aperture of $3 \times 3\ \text{mm}^2$. Five of these fibers, including the four located at the corners of the bundle are used for monitoring purposes outside of the vacuum chamber. The remaining 31 fibers ($\sim 4.5\ \text{m}$ long) are brought into the vacuum chamber, each with its own individual vacuum feedthrough. Each fiber is terminated by a ferrule made of carbon-reinforced plastic that is inserted into the machined receptacle in the Cs sensor. On average, each output fiber carries $\sim 1.4\%$ of the input fiber's power.

2. HV-compatible sensor modules

Seven Cs magnetometers were mounted on top of the HV electrode (Fig. 4) which was typically charged to $\pm 132\ \text{kV}$. Since a galvanic connection to ground is not permitted, we have opted for a fully opto-coupled operation. The light transmitted by the cell is not detected by a photodiode mounted next to the cell, but rather coupled into a $3\ \text{m}$ long $800\ \mu\text{m}$ diameter multimode fiber carrying the light to a photodiode mounted on the grounded vacuum tank. Tefzel[®] (dielectric constant 2.6) was selected as a fiber coating in order to allow good electrical isolation of the sensor. The RF signal driving the magnetic resonance is transmitted to the sensor by light with a sinusoidal power modulation (superimposed on a DC offset), that is generated by an IR LED (Lite-On Technology, model HSDL 4230) coupled to a $5\ \text{m}$ long $800\ \mu\text{m}$

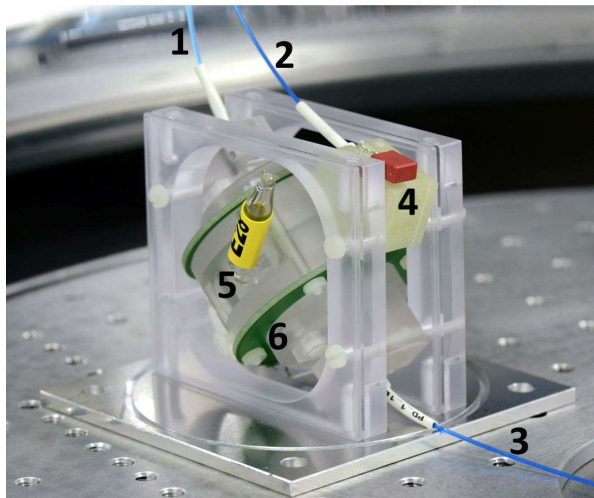


FIG. 4. HV-compatible magnetometer. The three fibers connected to the sensor provide the laser light (1), the RF signal (2), and collect the transmitted light (3). The Cs cell (of which only the sidearm, 5, is visible) is placed in a polycarbonate housing and surrounded by the RF coils printed on the (green) PCB boards (6). The photodiode and the capacitor forming the opto-coupler that drives the RF coils are mounted on a plastic holder (4).

multimode fiber. The plastic of the LED's case is ground down to a distance of $\sim 1-2$ mm from the semiconductor die and polished to optimize coupling into the fiber. Using a Si photodiode (Hamamatsu, model S6775-01) mounted near the sensor, the modulated light is transformed into a sinusoidal photocurrent that drives the RF coil via a non-magnetic 470 nF capacitor (WIMA 0.47 63/40) connected in series to suppress DC currents.

B. Phase-feedback mode of operation

1. Description

The magnetometer is operated in the M_x configuration [9, 24, 25] in which the precession of the Cs atoms' magnetization around \mathbf{B} is resonantly driven by a weak oscillating magnetic field $\mathbf{B}_{\text{RF}}(t) = \mathbf{B}_1 \sin(2\pi f_{\text{RF}} t)$. This radio-frequency (RF) field is produced by a pair of Helmholtz-like coils placed symmetrically around the cell (Fig. 3), such that $\hat{\mathbf{B}}_1 = \hat{\mathbf{k}}$, with \mathbf{k} the wave vector of the laser beam. The $\mathbf{B}_1 \parallel \mathbf{k}$ geometry avoids heading errors such that the shape and center of the resonance do not depend on the orientation of \mathbf{B} with respect to \mathbf{k} [25, 26].

The light absorption by the Cs vapor depends on the projection of the atoms' magnetization onto \mathbf{k} . The magnetization precesses at the driving frequency f_{RF} and thus the transmitted light power has a component $\delta P(t)$ modulated at that frequency

$$\delta P(t) = P_{\text{R}} \sin(2\pi f_{\text{RF}} t + \phi). \quad (6)$$

Here P_{R} is the modulation amplitude which depends on the light power, the degree of polarization, and the atomic absorption cross section. The phase ϕ is the phase difference with respect to the driving field \mathbf{B}_{RF} . It has a characteristic resonant behavior [25]

$$\phi_E = \phi - \phi_0 = -\arctan\left(\frac{f_{\text{RF}} - f_{\text{L}}}{\Gamma/2\pi}\right). \quad (7)$$

Here $\Gamma = 1/T_1 = 1/T_2$ is the spin relaxation rate which is assumed to be isotropic. In absence of any additional phase shifts in the electronic circuits, the reference phase ϕ_0 has the values of $\pm\pi/2$ depending on the direction of the magnetic field to be measured. The representation of the phase in Eq. (7) is chosen such that the variable ϕ_E has a zero-crossing in the center of the resonance at $f_{\text{RF}} = f_{\text{L}} = \gamma_4 B/2\pi$. Close to that point ϕ_E is proportional to the difference between the driving frequency and the Larmor frequency. Its slope with respect to a change of the magnetic field magnitude can thus be expressed as

$$\begin{aligned} \left. \frac{d\phi_E}{dB} \right|_{f_{\text{RF}}=f_{\text{L}}} &= -\left. \frac{d}{dB} \arctan\left(\frac{f_{\text{RF}} - \gamma_4 B/2\pi}{\Gamma/2\pi}\right) \right|_{f_{\text{RF}}=f_{\text{L}}} \\ &= \frac{\gamma_4}{\Gamma}. \end{aligned} \quad (8)$$

The phase ϕ_E is determined by a digital signal processing (DSP) system that generates the driving frequency f_{RF} via a digital-to-analog converter and samples the photocurrent of the photodiode via an analog-to-digital converter. For this, the photocurrent which is proportional to the light power transmitted through the Cs cell is converted to a voltage by a transimpedance amplifier, prior to digitization. The sampled voltage signal is then demodulated by a two-phase lock-in algorithm [25] that determines the amplitude of the oscillation and its phase. The reference phase ϕ_0 can be programmed via the digital interface of the DSP system which is also used to periodically read out the determined amplitude and phase values.

Figure 5 shows a measurement of ϕ as a function of f_{RF} . Such scans are used to determine the reference phase ϕ_0 which is necessary to compute the shifted phase ϕ_E . Phase shifts in the electronic circuits that are used in the generation of f_{RF} and the sampling of the photocurrent can cause changes in the reference phase ϕ_0 . The distinctive arctan line shape shown in Fig. 5 permits the determination of ϕ_0 independently of external references. This procedure thus constitutes an internal calibration and is performed periodically.

In normal operation f_{RF} is not scanned. It is rather controlled by a servo algorithm that uses ϕ_E as its error signal. If ϕ_0 was correctly determined, keeping $\phi_E = 0$ is equivalent to ensuring that $f_{\text{RF}} = f_{\text{L}}$. As a consequence, $f_{\text{RF}} - f_{\text{L}}$ – which is digitally synthesized in the DSP system – becomes a measure for the magnetic field which is periodically sampled directly in the DSP system. This mode of operation using a feedback loop is similar to standard phase-locked-loop schemes. Here, however, a frequency

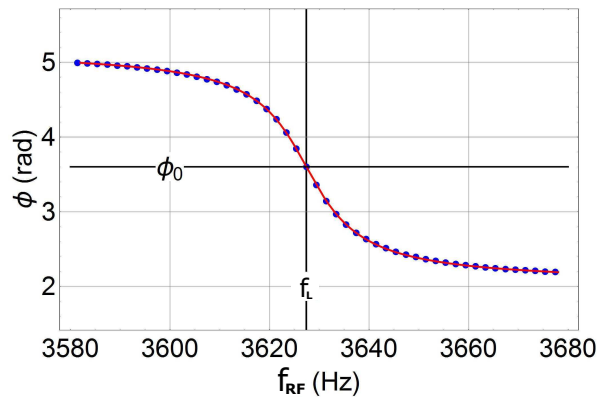


FIG. 5. Typical calibration curve of a Cs sensor shown with the fit using Eq. (7). The resulting fit parameters are: $\phi_0=3.6032(8)$ rad, $f_L=3619.980(8)$ Hz, and $\Gamma/2\pi=5.358(7)$ Hz.

offset does not result in a linearly changing error signal. Thus, in contrast to standard phase-locked loop systems, the error signal ϕ_E must not only be kept constant but also equal to zero in order to match f_{RF} and f_L . This means that an offset $\Delta\phi_E$ in the determination of ϕ_E translates to an offset in the measured magnetic field according to Eq. (8)

$$\Delta B = \left(\frac{d\phi_E}{dB}\right)^{-1} \Delta\phi_E = \frac{\Gamma}{\gamma_4} \Delta\phi_E. \quad (9)$$

2. Magnetometric sensitivity

The statistical uncertainty of the magnetic field measurement can be computed according to the propagation of noise from the sampled photocurrent I^{PD} . The phase noise spectral density is given by

$$\rho(\phi) = \frac{\rho(I^{PD})}{I_{RF}^{PD}}, \quad (10)$$

where I_{RF}^{PD} is the amplitude of the oscillation in the photocurrent at the applied RF frequency. Using Eq. (9) we find

$$\rho(B) = \frac{\Gamma\rho(\phi)}{\gamma_4} = \frac{\Gamma}{\gamma_4} \frac{\rho(I^{PD})}{I_{RF}^{PD}}. \quad (11)$$

In the shot noise limit, $\rho(I^{PD}) = \sqrt{2eI_{DC}^{PD}}$ with I_{DC}^{PD} the DC component of the photocurrent, the magnetometric sensitivity for all used sensors was better than $\rho(B) = 50 \text{ fT}/\sqrt{\text{Hz}}$ after an optimization of the light power and the B_{RF} amplitude. The shot noise limit was used as the figure of merit for this optimization since it can be computed independently of the external magnetic noise which depended significantly on the changing experimental environment. During nEDM measurements

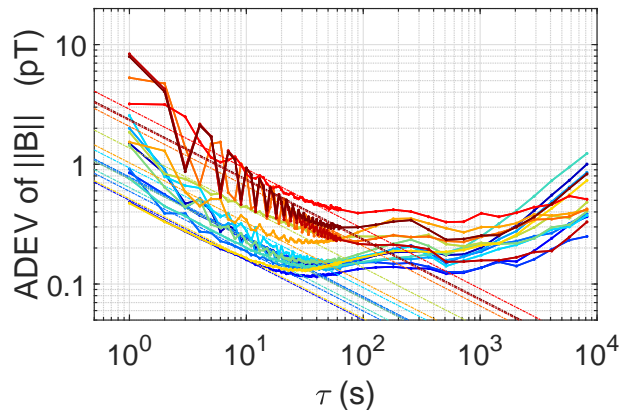


FIG. 6. Allan deviations of the magnetic field magnitude measured by 15 of the Cs magnetometers. The straight lines indicate the $\tau^{-1/2}$ behavior of pure white noise. The oscillations that are visible for some sensors are caused by the RF field of a neighboring sensor, as explained in the text.

the typical statistical sensitivity of the Cs magnetometers was $\rho(B) = 750 \text{ fT}/\sqrt{\text{Hz}}$. The increase in statistical noise was due to the aluminum shielding cans (thickness 2 mm) that had to be installed around each sensor to suppress interference from the B_{RF} fields of neighboring sensors. Even with the cans installed, a small amount of beating was observed due to the remaining interference. This is the reason why some magnetometers show a pronounced structure in the Allan deviations shown in Fig. 6. The resulting average sensitivity (including the beating effect) ranges from 0.75 to 8 pT/ $\sqrt{\text{Hz}}$.

3. Accuracy

One can distinguish two types of effects that influence the accuracy of the Cs magnetometer. The first relates to inaccuracies in determining the Larmor precession frequency f_L . The second category includes all effects that change f_L itself, modifying the relation between the Larmor precession frequency and the magnetic field as given by Eq. (5).

Below follows a short discussion of both types, concluding with recommendations on how to keep the offsets as stable as possible, allowing for high relative accuracy of the magnetic field reading.

As the extraction of the Larmor precession frequency relies heavily on the reference phase ϕ_0 , any drift of ϕ_0 without recalibration will worsen the accuracy of the sensor. Such drifts can occur due to temperature-related effects in the electronics or when, for example, the laser intensity changes [27] and thus the capacitance of the photodiode. In order to quantify such drifts in the nEDM Cs magnetometer array, we have performed calibrations before and after each nEDM run, typically 1 to 4 days apart. Figure 7(a) shows a histogram of the extracted

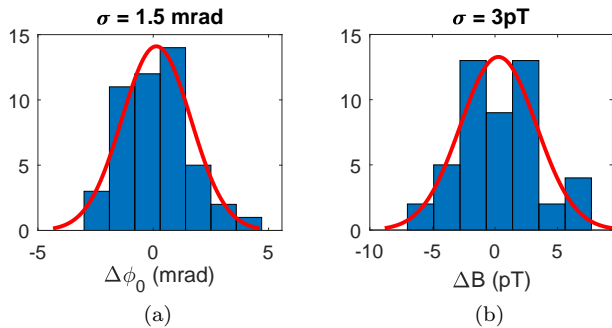


FIG. 7. (a) The difference in extracted reference phase ϕ_0 between two consecutive calibrations. The typical time between the two calibrations is 1 to 4 days. (b) The corresponding offset in the magnetic field reading, as calculated by Eq. (9). The distributions in (a) and (b) are not identical, as the width Γ in the conversion factor depends on the light intensity, which varies from sensor to sensor.

phase change $\Delta\phi_0 = \phi_{0,\text{after}} - \phi_{0,\text{before}}$ for one of the sixteen sensors. The typical change of reference phase is on the order of 1 to 2 mrad. An uncorrected drift $\Delta\phi_0$ of the on-resonance phase during phase-feedback operation results in an offset in the magnetic field measurement according to Eq. (9). Figure 7(b) shows the results of converting the phase differences in Fig. 7(a) to offsets in the magnetic field reading. The standard deviation of the magnetic field reading offset depends on the sensor properties and ranges from 1 to maximum 7 pT. This is of the same order of magnitude as the inherent uncertainty provided by the calibration procedure itself, which is about 1 pT.

Regarding the second category of inaccuracies, there are several effects that modify the Larmor precession frequency, or to be more precise, the energy separation of adjacent Zeeman sublevels of the $F=4$ ground state of the ^{133}Cs atoms. The resonance frequency that is measured by the Cs magnetometer in phase-feedback mode is a weighted average of the energy differences between the m and $m+1$ magnetic sublevels. In a system without laser interaction, the energy levels are the eigenvalues of the Cs ground state Hamiltonian containing the hyperfine interaction $A\mathbf{J} \cdot \mathbf{I}$ between the electronic spin \mathbf{J} and the nuclear spin \mathbf{I} , and the interaction of the magnetic moment with the applied magnetic field $\mu \cdot \mathbf{B}$. Applying perturbation theory to first order in $\mu B/A$ (for μB small compared to the scale given by the hyperfine structure constant A) then yields the linear Zeeman level splitting. The exact solution for this $J = 1/2$ system is given by the Breit-Rabi equation [28]. For a magnetic field of 1 μT , the nonlinear terms in the Zeeman effect result in a maximum deviation equivalent to 3 pT for neighboring magnetic sublevels, giving an upper limit on the inaccuracy due to nonlinear Breit-Rabi splitting.

A second effect of this category has to do with the use of a nonrotating driving field $\mathbf{B}_{\text{RF}} = \mathbf{B}_1 \sin(2\pi f_{\text{RF}}t)$. The nonrotating field produces a Bloch-Siegert shift [29,

30], which shifts the resonance by

$$\frac{(B_1 \sin \theta_B)^2}{16B_0} = \frac{B_1^2}{32B_0} \approx 0.5 \text{ pT}, \quad (12)$$

as the RF field of 4 nT makes an angle of $\theta_B = \pi/4$ with the main B_0 field of 1 μT .

Another interaction that modifies the energy of the magnetic sublevels is the AC Stark shift induced by the coherent laser light, otherwise known as the virtual light shift [31]. It entails an interaction $\mathbf{d} \cdot \mathbf{E}$ between the electric dipole moment operator \mathbf{d} of the Cs atoms and the oscillating electric field \mathbf{E} of the laser light. Apart from modifying the hyperfine splitting and the common energy of all levels, it also produces a linear splitting and a quadratic splitting of the magnetic sublevels. The former is called a vector light shift, the latter a tensor light shift. The vector light shift can be interpreted as an effective magnetic field that is oriented along the direction of the laser beam for σ^+ light. As the laser light propagates at an angle of 45° with respect to \mathbf{B} , this effective magnetic field will add or subtract to the magnitude of the main magnetic field, depending on the direction of \mathbf{B} . Both the vector and the tensor light shift in the $F_g=4$ ground state depend linearly on the intensity of the light and have a dispersive line shape relative to the laser detuning around each hyperfine transition. Although the dispersive function vanishes when the laser frequency is resonant with the respective transition $F_g=4 \rightarrow F_e=3$, the light shift itself does not, as the dispersive function of the neighboring transition $F_g=4 \rightarrow F_e=4$ is quite broad and nonzero at that laser frequency. In order to determine the size of this effect in the nEDM experiment, dedicated measurements were done by changing the intensity of the light in a controlled way and scanning the detuning of the laser around the $F_g=4 \rightarrow F_e=3$ transition. To avoid the inaccuracy issues of the first type, the magnetometers were run in the free spin precession (FSP) mode [32, 33]. This mode of operation consists of the following steps: (i) an initial polarization of the Cs atoms is created along \mathbf{B} by optical pumping with the circularly polarized laser beam oriented at 45° with respect to \mathbf{B} ; (ii) a resonant radio frequency pulse $\mathbf{B}_{\text{RF}} \parallel \mathbf{k}$ rotates the atomic spins to the transverse plane and causes them to precess around the magnetic field \mathbf{B} ; and (iii) the free precession of the Cs atoms is observed as they slowly spiral back to the \mathbf{B} -direction by monitoring the transmitted power of the laser beam. The advantage of operating the magnetometer in the FSP mode is that one directly detects the Larmor spin precession frequency f_L of the Cs atoms. These FSP studies [34] have shown that the sensors display shifts ranging from ± 10 pT to ± 50 pT at their typical light intensities, which are correlated to the light intensity, depend on the laser detuning and indeed change sign as the magnetic field is reversed. The FSP mode of operation was only used to test the Cs magnetometers since the pulse repetition frequency is close to the Larmor frequency of the ^{199}Hg atoms. Oscillating magnetic fields with frequency components close to the resonance

TABLE I. Overview of effects that relate to inaccuracies in determining the Larmor precession frequency f_L (line 1), or that change f_L itself (lines 2 to 5) thereby modifying the relation between the Larmor precession frequency and the magnetic field as given in Eq. (5).

Effect	size (pT)
Reference phase drifts	1 to 7
Quadratic Zeeman splitting	3
Bloch-Siegert shift	0.5
Vector light shift	10 to 50
Spin exchange	<30

frequency can cause changes in the Larmor precession of the ^{199}Hg atoms via the Ramsey-Bloch-Siegert shift which was not acceptable during nEDM data taking. Recent implementations of the FSP mode avoid interference via the RF field by using all-optical designs [32].

A fourth effect that modifies the Hamiltonian of the atom-light system is due to spin-exchange collisions between the ^{133}Cs atoms [35, 36]. The frequency shift operator contains a term proportional to $\mathbf{S} \cdot \langle \mathbf{S} \rangle$, where \mathbf{S} is the electron spin of the Cs atoms. This effect scales with the number density of the alkali atoms [37] and is therefore exponentially dependent on temperature. The exact implications for our magnetometer are not yet fully understood theoretically, but preliminary measurements comparing the precession frequency in different parts of the FSP signal (and thus at different directions of $\langle \mathbf{S} \rangle$) seem to indicate that the effect is smaller than 30 pT for all sixteen sensors [34].

An overview of the effects discussed above is given in Table I. Combining the values of the different effects, the absolute accuracy of the sensors adds up to be in a range from 45 to 90 pT. For the purpose of measuring drifts of the vertical magnetic field gradient G_{grav} , the absolute accuracy of the magnetometers is not crucial, but it is important that the relative reading offsets of all sensors remain stable in time. It is therefore recommended to keep the light intensity sufficiently stable to avoid drifts in the reference phase and to keep the light shift in check. Additionally, large changes in temperature should be avoided, both for the stability of the electronics and the spin exchange effect. The achieved stability in the nEDM experiment was significantly better than the requirements for time scales up to 10000 s as discussed in section IV A.

C. Variometer method

The array of Cs magnetometers can be used to obtain the vector components of the magnetic field by applying the variometer principle [21]. The implementation of this method will be explained in Section III C 1, its sensitivity and accuracy will be discussed in Sections III C 2 and III C 3 respectively.

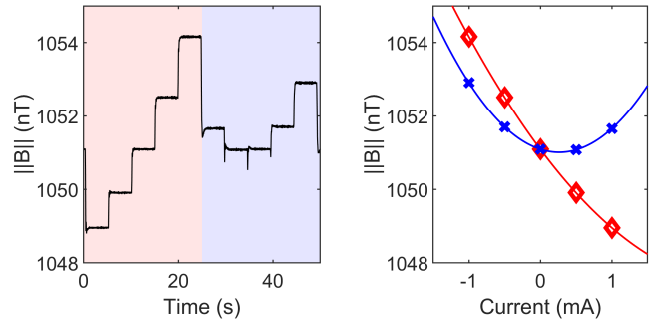


FIG. 8. On the left: the response of one of the Cs magnetometers to a current pattern of 1, 0.5, 0, -0.5 and -1 mA in steps of 5 s, first applied to a coil in the x -direction (0–25 s indicated in red), then to a coil in the y -direction (25–50 s indicated in blue). The main field of $1.051 \mu\text{T}$ is maintained along the z -direction. A current of 1 mA corresponds to an applied field of about 50 nT. On the right: the corresponding parabolic behavior of the magnitude as a function of the applied current to a coil in the x -direction (red diamonds) and a coil in the y -direction (blue crosses).

1. Working principle

The variometer method consists of applying a well known magnetic field \mathbf{B}_T transverse to the main magnetic field of $1 \mu\text{T}$. Using the Cs magnetometers in phase-feedback mode to measure the magnitude of the total magnetic field, the additional transverse magnetic field changes the magnitude to:

$$\|\mathbf{B}_0 + \mathbf{B}_T I\|^2 = \|\mathbf{B}_0\|^2 + 2\mathbf{B}_0 \cdot \mathbf{B}_T I + \|\mathbf{B}_T\|^2 I^2, \quad (13)$$

where \mathbf{B}_0 represents the main magnetic field, I the current applied to the transverse coil, and \mathbf{B}_T the field produced by this transverse coil at the position of the Cs magnetometer when applying one unit of current. Probing the field magnitude with a set of different currents, one can extract $\|\mathbf{B}_0\|$, $\|\mathbf{B}_T\|$ and $\mathbf{B}_0 \cdot \mathbf{B}_T$ from the quadratic behavior of $\|\mathbf{B}_0 + \mathbf{B}_T I\|^2$ as a function of the current. The scalar product $\mathbf{B}_0 \cdot \mathbf{B}_T$ contains the angle between the applied transverse magnetic field and the main field \mathbf{B}_0 . Projecting on two known transverse magnetic field directions, one can reconstruct the direction of \mathbf{B}_0 .

An example of the readout of a Cs sensor during the application of the variometer method is shown in Fig. 8. Here, a sequence of five equally spaced currents is applied for five seconds each, first to a coil in the x -direction, then to a coil in the y -direction, whereas the main magnetic field is maintained in the z -direction. The currents are applied with an Agilent 33500B function generator, using a resistor of $10 \text{ k}\Omega$ in series with the transverse coils to convert the voltage generated by the function generator to a proportional current. In order to avoid magnetization of the μ -metal shield, the maximal current I is chosen such that the transverse field is about a factor of 20 smaller than the main magnetic field of $1 \mu\text{T}$. This

results in a change of the magnetic field magnitude by typically 5 nT. As the Cs magnetometer is run in the phase-feedback mode, the reaction of the sensor to this sudden change of the magnetic field is not instantaneous, but has a time constant of a few 100 ms, depending on the parameters of the stabilizing PID algorithm. Consequently, the ramping parts of the signal have to be cut when averaging the magnitude over one current setting, effectively increasing the measurement uncertainty calculated in Section III C 2.

In order to extract the vector components of the main magnetic field, knowledge of the direction of the applied transverse field is crucial. The coils that are used to generate \mathbf{B}_T are normally used for applying the UCN and ^{199}Hg $\pi/2$ spin-flip pulses in the nEDM experiment. The magnetic fields produced by these coils were measured in 2014 with a nonmagnetic mapping device – the topic of the third episode in the trilogy – consisting of a three-axis fluxgate magnetometer mounted on a trolley. The trolley could move along a horizontal arm, which itself could rotate along a vertical axis and move up and down along the same vertical axis. Scanning the volume in discrete steps, the magnetic field map can be reconstructed from the corresponding fluxgate readings [38]. The resulting accuracy of these field maps at the specific Cs magnetometer positions is about 1 nT on each magnetic field component for a 50 nT total field produced by the coil.

This 2% inaccuracy of the field maps translates into a similar inaccuracy of all three vector components of \mathbf{B}_0 if the extraction is based purely on the two transverse projections. For this reason, we additionally include the fact that the magnetic field is predominantly homogeneous and assume that the B_{0z} component of the main field is closely approximated by the field magnitude $B_{0z} = \pm \|\mathbf{B}_0\|$ (true at the tens-of-pT level), with the sign being determined by the set B_0 direction. Using this approximation, one can extract B_{0x} and B_{0y} by solving the following set of equations:

$$\begin{bmatrix} \mathbf{B}_0 \cdot \mathbf{B}_1 - B_0 B_{1z} \\ \mathbf{B}_0 \cdot \mathbf{B}_2 - B_0 B_{2z} \end{bmatrix} = \begin{bmatrix} B_{1x} & B_{1y} \\ B_{2x} & B_{2y} \end{bmatrix} \begin{bmatrix} B_{0x} \\ B_{0y} \end{bmatrix}, \quad (14)$$

where \mathbf{B}_1 and \mathbf{B}_2 are the two applied transverse fields. To take into account slight differences in applied currents during the maps and the variometer measurement, the \mathbf{B}_1 and \mathbf{B}_2 maps are scaled using the $\|\mathbf{B}_T\|^2$ parameter from the quadratic fit in Eq. (13). Matrix inversion of Eq. (14) yields

$$\begin{aligned} B_{0x} &= \frac{B_{2y}(\mathbf{B}_0 \cdot \mathbf{B}_1 - B_0 B_{1z}) - B_{1y}(\mathbf{B}_0 \cdot \mathbf{B}_2 - B_0 B_{2z})}{B_{1x}B_{2y} - B_{2x}B_{1y}} \\ &\approx \frac{\mathbf{B}_0 \cdot \mathbf{B}_1 - B_0 B_{1z}}{B_{1x}} \end{aligned} \quad (15)$$

and

$$\begin{aligned} B_{0y} &= \frac{B_{1x}(\mathbf{B}_0 \cdot \mathbf{B}_2 - B_0 B_{2z}) - B_{2x}(\mathbf{B}_0 \cdot \mathbf{B}_1 - B_0 B_{1z})}{B_{1x}B_{2y} - B_{2x}B_{1y}} \\ &\approx \frac{\mathbf{B}_0 \cdot \mathbf{B}_2 - B_0 B_{2z}}{B_{2x}}, \end{aligned} \quad (16)$$

where the second lines are obtained by assuming that B_{1y} and B_{2x} are negligible (meaning \mathbf{B}_1 is oriented predominantly along x and \mathbf{B}_2 predominantly along y). It is worth noting here that the statistical uncertainties on B_{0x} and B_{0y} originate from the terms proportional to the scalar products, whereas the accuracy is determined by the terms proportional to $B_0 B_{1z}$ and $B_0 B_{2z}$.

2. Magnetometric sensitivity

Based on the second line of Eqs. (15) and (16), the statistical uncertainty of the variometer method during one measurement cycle is determined by

$$\sigma(B_{0j}) = \frac{\sigma(\mathbf{B}_0 \cdot \mathbf{B}_T) - \sigma(B_0)B_{Tz}}{B_{Tj}}, \quad (17)$$

with j indicating the direction of the transverse coil producing \mathbf{B}_T . The components of \mathbf{B}_T do not introduce a statistical uncertainty, as they are fixed by the magnetic field maps. The precision with which the scalar product between \mathbf{B}_0 and \mathbf{B}_T can be determined depends on the amplitude and the duration of the currents applied to the transverse coils. Let us consider the case of a sequence of n steps of equal duration T with applied currents I_i , assuming an anti-symmetric sequence of currents: $\sum_i I_i = 0$. The uncertainty on the square of the magnetic field magnitude during one step is then given by $\sigma(B^2) = 2B\sigma(B) = 2B\frac{\rho(B)}{\sqrt{2T}}$, with $\rho(B)$ the noise density of the magnitude (Eq. (11)). Using weighted linear least squares fitting, the uncertainty on the coefficient of the linear term in Eq. (13) is given by

$$\sigma(2\mathbf{B}_0 \cdot \mathbf{B}_T) = \frac{\sigma(B^2)}{\sqrt{\sum_{i=1}^n I_i^2}} = \frac{2B\rho(B)}{\sqrt{2T}\sqrt{\sum_{i=1}^n I_i^2}}. \quad (18)$$

As B_{Tz} is typically not larger than a few nT, the uncertainty on the scalar product $\sigma(\mathbf{B}_0 \cdot \mathbf{B}_T)$ is about a factor of 1000 larger than $\sigma(B_0)B_{Tz}$, hence one can neglect the second term in Eq. (17). The uncertainty during one measurement cycle is then

$$\sigma(B_{0j}) = \frac{B}{B_{Tj}} \frac{\rho(B)}{\sqrt{2T}} \frac{1}{\sqrt{\sum_{i=1}^n I_i^2}}. \quad (19)$$

Taking into account that two transverse projections are needed, the duration of one full variometer measurement

cycle is $2nT$, hence giving the following noise density:

$$\rho(B_{0j}) = \sigma(B_{0j})\sqrt{4nT} = \rho(B) \frac{B}{B_{Tj}} \frac{\sqrt{2n}}{\sqrt{\sum_{i=1}^n I_i^2}}. \quad (20)$$

It is clear that in order to get the best sensitivity, one has to use the smallest number of steps $n = 3$ (I , 0 and $-I$) per transverse field direction at the highest possible current I . A typical variometer measurement cycle for the nEDM experiment then consists of applying a sequence of 3 steps of 6 s per transverse direction with a maximum applied transverse field of 50 nT. Such a measurement typically results in an uncertainty of about 10 pT, which is about a factor of 3 larger than expected from the calculated noise density. The reason is that, at this level of precision, the stability of the current source is a limiting factor. The uncertainty on the squared magnitude of the field should thus be modified to

$$\sigma(B^2) = \sqrt{\left(2B\sigma(B)\right)^2 + \left(\sigma(I) \frac{\partial B^2}{\partial I}\right)^2}, \quad (21)$$

such that the μA precision of the current source can be taken into account.

3. Stability and accuracy

The accuracy of the variometer method is determined by the accuracy of the field maps of \mathbf{B}_1 and \mathbf{B}_2 at the positions of the Cs sensors. These maps typically have an inaccuracy of 1 nT in all three components. Particularly the inaccuracy of the z -component propagates into a systematic error in B_{0x} and B_{0y} through the terms $B_0 B_{1z}/B_{1x}$ and $B_0 B_{2z}/B_{2x}$ of Eqs. (15) and (16) respectively. Using typical values of 1 μT for B_{0z} and 50 nT for B_{1x} and B_{2y} , the estimated accuracy is 20 nT. Fortunately, the z -component fares much better, since it is nicely approximated by the magnitude. If the transverse components remain smaller than 10 nT, as is typically the case in the nEDM experiment, the error made with this approximation is less than 100 pT.

Luckily, the inaccuracy due to the $B_{0z}B_{Tz}/B_{Tj}$ term is canceled when comparing two variometer measurements of similar main magnetic fields. Assuming the main magnetic field direction is not changed too much, the difference between two magnetic fields can be determined with a relative accuracy of a few percent, since the main contribution of B_{0z} to the 20 nT cancels out when taking a difference. This of course does not hold when inverting the magnetic field direction. As shown in Section IV, these relative measurements are very useful for characterizing drifts of the main magnetic field and provide access to higher order magnetic field gradients that are inaccessible with the regular phase-feedback mode.

IV. APPLICATIONS OF THE MAGNETOMETER ARRAY

The Cs magnetometer array can be used for a variety of applications. The remainder of this paper will focus on two important ones directly beneficial to the nEDM experiment: (i) the implementation of a strategy to correct for the drift of the vertical magnetic field gradient and (ii) a procedure to optimize the homogeneity of the magnetic field. Section IV A describes how to extract the magnetic field gradients from the magnetometer array when vector or scalar magnetic field information is collected. This procedure is then applied to the data taken during the nEDM experiment to characterize the typical gradient drifts and to estimate the accuracy of the gradient extraction that is solely based on the magnitude readings. Section IV B outlines the optimization procedure that significantly improved the sensitivity of our nEDM experiment during the 2015 and 2016 data taking campaigns.

A. Spatial field distribution and gradient extraction

In order to extract the magnetic field gradients, we need a convenient model to describe the spatial field distribution in the nEDM experiment. We use the multipole expansion as presented in [5], where the magnetic field at position \mathbf{r} is expanded in the form:

$$\mathbf{B}(\mathbf{r}) = \sum_{l,m} G_{l,m} \begin{bmatrix} \Pi_{x,l,m}(\mathbf{r}) \\ \Pi_{y,l,m}(\mathbf{r}) \\ \Pi_{z,l,m}(\mathbf{r}) \end{bmatrix}, \quad (22)$$

with the $\Pi_{l,m}$ harmonic polynomials of degree l in the Cartesian coordinates x , y and z , and $G_{l,m}$ the corresponding gradient coefficients. Each degree l has $2l + 3$ polynomials, with m ranging from $-(l + 1)$ to $l + 1$. The origin of the coordinate system is chosen at the center of the cylindrical precession chamber, as this significantly simplifies averaging over the chamber volume. The harmonic polynomials up to third order are listed in Table II of [5].

The gradient G_{grav} – introduced in Eq. (3) – that is relevant for the nEDM experiment, is a specific combination of the harmonic coefficients [5]:

$$G_{\text{grav}} = G_{1,0} + G_{3,0} \left(\frac{3H^2}{20} - \frac{3R^2}{4} \right), \quad (23)$$

where H is the height and R the radius of the cylindrical storage chamber. Plugging in the dimensions of the nEDM precession chamber, the vertical gradient is given by $G_{\text{grav}} = G_{1,0} - G_{3,0}(393 \text{ cm}^2)$.

1. Gradient extraction in the variometer mode

If the vector components of the magnetic field are known at positions \mathbf{r}_i , the gradients $G_{l,m}$ can be determined by solving the matrix equation

$$\begin{bmatrix} B_x \\ B_y \\ B_z \end{bmatrix} = \begin{bmatrix} \Pi_x \\ \Pi_y \\ \Pi_z \end{bmatrix} G, \quad (24)$$

where B_x is a column vector with elements B_x^i representing the x -component of the magnetic field measured at positions \mathbf{r}_i , Π_x is a matrix with elements $(\Pi_x)^{ij} = \Pi_{x,l_j,m_j}(\mathbf{r}_i)$, i.e., the harmonic polynomial defined by l_j and m_j evaluated at position \mathbf{r}_i , and G is a column vector containing the harmonic coefficients G_{l_j,m_j} . The expressions are similar for the y - and z -matrices. In the particular case of measurements with the variometer method there is, however, a significant difference between the uncertainty on B_z and the uncertainties on the transverse components B_x and B_y . Therefore, each line in the matrix equation is weighted with the inverse of the squared uncertainty of the corresponding magnetic field component value. In order to accommodate for the inaccuracies of the variometer method, the error estimation on the harmonic coefficients $G_{l,m}$ is always scaled with the square root of the χ^2/ν of the fit.

Since one of the HV-compatible magnetometers failed after an electrical discharge burned one of its optical fibers at an early stage of data taking, we only have 15 sensors available to fit the harmonic coefficients. This results in $3 \times 15 = 45$ equations, enabling us to comfortably fit up to third order (24 harmonics) while still having enough degrees of freedom for error estimation. This means that the harmonic coefficients necessary for the estimation of G_{grav} are easily accessible using the variometer method. However, since the method involves applying additional magnetic fields, it is not used during a typical nEDM measurement cycle as it would disturb the neutron EDM measurement.

2. Gradient extraction in the phase-feedback mode

Since in phase-feedback mode only the magnitude of the magnetic field is known at positions \mathbf{r}_i , we first have to make the following approximation:

$$\pm \|\mathbf{B}\| = B_z + \frac{B_x^2 + B_y^2}{2B_z} + \dots \approx B_z, \quad (25)$$

where the sign is determined by the main direction of \mathbf{B} , which is oriented along the z -axis. This approximation is valid in the nEDM experiment as the field maps have shown that the transverse components of the main 1 μT field are typically smaller than 10 nT. To extract the magnetic field gradients $G_{l,m}$, one has to solve the matrix equation $B_z = \Pi_z^S G^S$, with the matrices being defined as in Eq. (24), with the exception that the polynomials

with $m_j = \pm(l_j + 1)$ are not included. The reason for this is that these modes are purely transverse and do not contribute to B_z , and are therefore not accessible via the magnitude. The superscript S (scalar) is added to make a clear distinction between gradients G determined from vector measurements and gradients G^S extracted from scalar measurements. Again, the uncertainty on the magnitude measurements can be used to assign weights to the equations.

As the nEDM experiment has sixteen Cs magnetometers, we typically limit the scalar harmonic expansion to second order (with 9 fit parameters), providing the following magnetic field description:

$$\begin{aligned} B_z(x, y, z) = & G_{0,0}^S + y G_{1,-1}^S + z G_{1,0}^S + x G_{1,1}^S \\ & + 2xy G_{2,-2}^S + 2yz G_{2,-1}^S \\ & + \left(z^2 - \frac{1}{2}(x^2 + y^2) \right) G_{2,0}^S \\ & + 2xz G_{2,1}^S + (x^2 - y^2) G_{2,2}^S. \end{aligned} \quad (26)$$

It is clear that the cubic vertical gradient $G_{3,0}$ is not directly accessible with this Cs magnetometer mode. However, the higher order terms do affect the extracted scalar gradients G^S . Assuming a multipole expansion $B_z = \Pi_z G$, the contribution of the higher order terms to the scalar fit parameters can be calculated explicitly:

$$G^S = \left((\Pi_z^S)^T W \Pi_z^S \right)^{-1} (\Pi_z^S)^T W \Pi_z G, \quad (27)$$

where W is a diagonal matrix containing the weight of each equation. Using the positions of the 15 Cs magnetometers that were operational during the 2015/2016 nEDM data taking and assuming equal weights for each magnetometer, the influence of the third order gradients on the vertical linear gradient $G_{1,0}^S = \sum a_{l,m} G_{l,m}$ is summarized in Table II. Adding weights based on the uncertainty changes the factors for each $G_{3,m}$, but the contribution of $G_{3,0}$ remains about 3/4 of the factor in Eq. (23), making $G_{1,0}^S$ a reasonable but slightly inaccurate estimator for G_{grav} .

3. Gradient extraction during nEDM data taking

In order to show that the Cs magnetometer array meets the requirements for gradient drift correction outlined at the end of Section II, we have to quantify the sensitivity and accuracy of the gradient extraction procedure based on the real magnetic field conditions in the nEDM experiment. To monitor the magnetic field during nEDM data taking, the typical measurement procedure regarding the Cs sensors consists of: (i) calibrations before and after each nEDM run to monitor the light intensity and the reference phase of the phase-feedback mode, (ii) followed by variometer measurements to monitor the higher order gradient drifts, and (iii) continuous measurements in the phase-feedback mode during the nEDM run. A

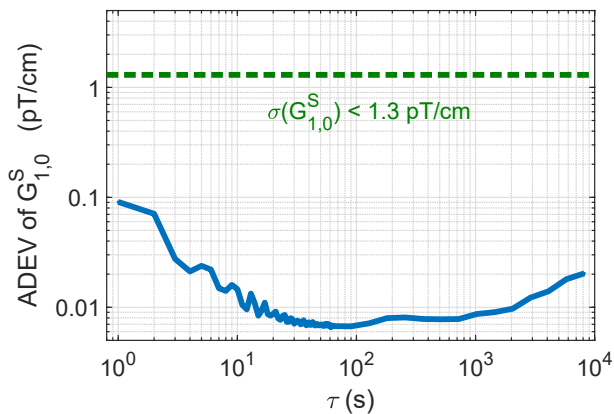


FIG. 9. The Allan deviation of the vertical gradient $G_{1,0}^S$ extracted from the data shown in Fig. 6 using the model in Eq. (26) is shown in blue. The achievable statistical uncertainty at the nEDM cycle duration of 180 s is 8 fT/cm, which is significantly below the upper limit indicated as a dashed green line. Statistical uncertainties in the magnetometers cause the rising slope towards small τ values. The result at 180 s is not limited by the slope but rather by the stability of the measurement system.

run typically takes a few days, corresponding to about 500 Ramsey cycles which each take five minutes, while the electric field is reversed every 56 cycles.

In order to quantify the gradient drift sensitivity during a Ramsey cycle, we extract $G_{1,0}^S$ from the data used in Fig. 6 and calculate its Allan deviation (ADEV). The results are shown in Fig. 9. It is clear that the realized gradient sensitivity during the neutron storage time of 180 s is significantly better than the requirement of 1.3 pT/cm calculated in Section II. The ADEV slowly increases for longer integration times but remains far below the limit for all relevant time-scales.

Regarding the accuracy of the gradient drift measurement, there are two effects that play a role. On the one hand there are sensor-related drifts that translate into an artificial gradient drift, on the other hand there are drifts of $G_{1,0}^S$ induced by changes in the higher order magnetic field gradients. To estimate the former, we compare the calibrations before and after each nEDM run, to characterize the latter, we use the variometer measurements.

As discussed in Section III B 3, the typical change in reference phase between calibration pairs before and after an nEDM run results in reading offsets corresponding to a few pT. Using the magnetic field gradient model of Section IV A 2, these offsets produce a change of the fit-parameter $G_{1,0}^S$ with a standard deviation of 0.1 pT/cm in the time span of a few days. Similarly, the light intensity changes slightly over the course of an nEDM run, modifying the light shift in each sensor, resulting in an artificial gradient drift with standard deviation of 0.03 pT/cm. Since the light intensity typically decreases over time and the direction of the laser beams is opposite for the sensors above and below the storage chamber, the average

TABLE II. Overview of the harmonic coefficients contributing to the fit parameter $G_{1,0}^S = \sum a_{l,m} G_{l,m}$ up to degree 3. For each harmonic coefficient $G_{l,m}$, the weighing factor $a_{l,m}$ and the standard deviation of the gradient drift $\sigma(\Delta G_{l,m})$ during a typical nEDM run are given. Taking into account the correlations between the different contributions, an estimation of the standard deviations of the drift of $G_{1,0}^S$ and its accuracy $G_{1,0}^S - G_{\text{grav}}$ are given in the last two lines.

$G_{l,m}$	$a_{l,m}$ (cm^{l-1})	$\sigma(\Delta G_{l,m})$ (pT/cm ^l)
$G_{1,0}$	1	1.71
$G_{3,-3}$	-135	0.0009
$G_{3,-2}$	344	0.0006
$G_{3,-1}$	22	0.0015
$G_{3,0}$	-288	0.0023
$G_{3,1}$	-23	0.0010
$G_{3,2}$	466	0.0010
$G_{3,3}$	1	0.0017
$G_{1,0}^S$		1.4–1.7
$G_{1,0}^S - G_{\text{grav}}$		< 0.7

change is about -0.01 pT/cm.

Comparing the variometer measurements before and after each nEDM run, we can extract the total change of each gradient $\Delta G_{l,m}$ during the run. The distribution of $\Delta G_{l,m}$ is Gaussian, with the standard deviation of the terms relevant to $G_{1,0}^S$ summarized in Table II. Taking into account the correlation between the drifts of $G_{1,0}$ and $G_{3,0}$, and using Eq. (23), the standard deviation of ΔG_{grav} is 1.4 pT/cm. Using the magnitude of the same data, the extracted drift of $G_{1,0}^S$ is in agreement with the drift of G_{grav} within the error bars of the parameters, which are typically 0.7 pT/cm for G_{grav} due to the inaccuracy of the variometer mode. This gives an upper limit on the relative accuracy of $G_{1,0}^S$: the accuracy is at least a factor of 2 better than the standard deviation of the drift on the timescale of an nEDM run. It follows that the dominant uncertainty on the extracted gradients is not due to the accuracy of the individual sensors, but rather due to the ‘aliasing effect’ of the higher order modes which are not included in the fit.

B. Homogenization of the magnetic field

The homogeneity of the magnetic field influences both the statistical precision of the nEDM experiment and its systematic effects. To improve the former without exacerbating the latter, we have developed a procedure for optimizing the magnetic field in the precession chamber. The principles behind this optimization strategy are explained in Section IV B 1. The implementation of the routine is described in Section IV B 2, followed by a discussion of the tuning of the algorithm in Section IV B 3. Finally, the resulting improvement in sensitivity is presented in Section IV B 4.

1. Principles behind the optimization

Improving the statistical sensitivity and minimizing the systematic effects impose different requirements on the magnetic field optimization.

The magnetic-field-related contribution to the statistical precision of the nEDM measurement is captured in the parameter α of Eq. (1), which is the visibility or contrast of the Ramsey resonance. This parameter is predominantly defined by the neutrons' transverse spin relaxation time T_2 via $\alpha(T) = \alpha_0 \exp(-T/T_2)$ where α_0 is the polarization at the start of the Ramsey procedure and T the precession time of the neutrons. The transverse relaxation time results from a combination of three types of neutron depolarization in the storage chamber, as discussed in [5]. The first mechanism is depolarization due to wall collisions, which is an effect that does not depend on the magnetic field. The second is gravitationally enhanced depolarization [39, 40], which is caused by the extremely low kinetic energy of the ultracold neutrons. Different energy groups of neutrons have a different average height in the chamber, so in the presence of a vertical magnetic field gradient their precession frequencies differ slightly. This causes a dephasing of the different energy groups, which results in a lower polarization at the end of the Ramsey procedure. To reduce this effect, it is crucial to minimize the vertical gradient of the longitudinal field component. The third mechanism is intrinsic depolarization, which refers to the depolarization within each given energy group. Even though the neutrons have the same energy, their trajectories through the chamber differ, resulting in dephasing if the magnetic field is not homogeneous over the chamber volume. Since the neutrons probe the field adiabatically while precessing in the transverse plane, the homogeneity of the longitudinal magnetic field component is key, whereas gradients of the transverse components play a negligible role.

Conversely, the magnetic-field-related systematic effects that are not dealt with in the extension of the *crossing point analysis* of [5], involve the quantities $\langle B_T^2 \rangle$ and $G_{3,0}$. The first is defined as

$$\langle B_T^2 \rangle = \left\langle (B_x - \langle B_x \rangle)^2 + (B_y - \langle B_y \rangle)^2 \right\rangle \quad (28)$$

and stands for the square of the transverse magnetic field components averaged over the storage volume. It is a second order combination of the harmonic expansion coefficients $G_{l,m}$:

$$\langle B_T^2 \rangle = \sum a_{ij} G_{l_i, m_i} G_{l_j, m_j}. \quad (29)$$

The coefficients a_{ij} are given in Appendix B of [5]. The smaller the gradients of the transverse magnetic field components, the smaller this systematic effect. The quantity $G_{3,0}$ is the cubic vertical gradient of the magnetic field model presented in Section IV A, and the related systematic effect decreases when the longitudinal homogeneity increases.

In summary, the precision improves when the longitudinal homogeneity is increased, and systematic effects are reduced when both the transverse homogeneity and the longitudinal homogeneity are increased.

2. Implementation

Firstly, the homogeneity of the longitudinal component of the magnetic field can be directly accessed by the Cs magnetometer array. However, since the sensors are not perfectly accurate and require off-line corrections, the longitudinal components are only available up to an accuracy of about 45 to 90 pT during on-line data taking (Table I). Therefore, the goal of the optimization routine is to reduce the spread of the Cs magnetometer readings to this level. Secondly, the transverse components are accessible with the variometer method, but the accuracy is not sufficient to keep $\langle B_T^2 \rangle$ below the goal of 2 nT^2 , which would correspond to a systematic effect at the level of a few $10^{-27} e \cdot \text{cm}$. For this reason, off-line field maps – that were recorded before the period of nEDM data taking – are used to provide a rough estimate of $\langle B_T^2 \rangle$. The final correction of this systematic effect will be performed with more accurate values extracted from a more recent mapping campaign (the analysis of which will be included in the third part of the trilogy).

Combining the on-line information of the Cs sensors with the off-line magnetic field maps, we developed a routine to optimize the currents I_{coil} applied to a set of 30 trim-coils wound around the vacuum tank. The magnetic field produced by each coil when applying one unit of current was characterized both on-line and off-line, providing $\mathbf{B}_{\text{coil}}^{\text{CsM}}$ measured by the Cs magnetometer (CsM) in the variometer mode, and the harmonic expansion coefficients $G_{\text{coil}}^{\text{map}}$ as extracted from the magnetic field maps. After measuring the main magnetic field $\mathbf{B}_0^{\text{CsM}}$ on-line with the Cs magnetometer array, the optimal currents are calculated by minimizing the sum of the following three terms:

$$S = S_{\text{Long}} + T_{\text{Trans}} S_{\text{Trans}} + T_{\text{Reg}} S_{\text{Reg}}, \quad (30)$$

where $S_{\text{Long}}(I_{\text{coil}})$ quantifies the homogeneity of the longitudinal component, $S_{\text{Trans}}(I_{\text{coil}})$ evaluates the systematic effect due to the transverse components and $S_{\text{Reg}}(I_{\text{coil}})$ is added as a regularization term since there are more parameters than constraints ($30 > 16+1$). The factors T_{Trans} and T_{Reg} are tuning parameters and assign a weight to the respective sums relative to S_{Long} .

The explicit expression for S_{Long} as a function of the currents I_{coil} is given by

$$S_{\text{Long}} = \sum_{\text{CsM}} \left(B_{0,z}^{\text{CsM}} + \sum_{\text{coil}} I_{\text{coil}} B_{\text{coil},z}^{\text{CsM}} - B_{\text{goal}} \right)^2, \quad (31)$$

where $B_{0,z}^{\text{CsM}}$ and $B_{\text{coil},z}^{\text{CsM}}$ are the z -components measured by the Cs magnetometer of the main magnetic field and

the field produced by the coil when applying one unit of current respectively. B_{goal} is the goal value for the Cs sensor magnitude readings. Typically, the sensors are all assigned the same goal value to improve the homogeneity, but other configurations are possible.

The transverse requirements are taken into account by the following sum

$$S_{\text{Trans}} = \langle (B_{\text{T}}^{\text{map}})^2 \rangle = \sum_{i,j} a_{ij} G_{l_i, m_i}^{\text{map}} G_{l_j, m_j}^{\text{map}}, \quad (32)$$

where $G_{l_i, m_i}^{\text{map}} = G_{0, l_i, m_i}^{\text{map}} + \sum_{\text{coil}} I_{\text{coil}} G_{\text{coil}, l_i, m_i}^{\text{map}}$ is the harmonic coefficient G_{l_i, m_i} of the total magnetic field that would be produced if the currents I_{coil} would be applied to the coils as determined from the field maps. The coefficients a_{ij} are defined in [5].

The regularization term is given by

$$S_{\text{Reg}} = \sum_{\text{coil}} \left(I_{\text{coil}} \max_{\text{CsM}} (\|\mathbf{B}_{\text{coil}}^{\text{CsM}}\|) \right)^2, \quad (33)$$

where $\max_{\text{CsM}} (\|\mathbf{B}_{\text{coil}}^{\text{CsM}}\|)$ is the maximum magnitude measured by the Cs magnetometers when one unit of current is applied to the coil. This term makes sure that the produced magnetic field per coil is not too large, avoiding a loss in sensitivity due to local inhomogeneities created by the coils themselves.

In order to minimize Eq. (30), we solve the set of equations $\partial S / \partial I_{\text{coil}} = 0$. Since the terms in S are at most of order 2 in I_{coil} , $\partial S / \partial I_{\text{coil}}$ is of order 1 and can be solved efficiently using matrix inversion.

3. Optimizing the tuning parameters

The success of the algorithm is determined by the choice of the tuning parameters T_{Trans} and T_{Reg} . To determine the optimal values, we start off with an estimate of the optimal size of each sum in Eq. (30). Given the on-line accuracy of the Cs magnetometers, we estimate the final standard deviation of $(B_z^{\text{CsM}} - B_{\text{goal}})$ at 100 pT, resulting in a longitudinal term S_{Long} of $(0.1 \text{ nT})^2 \times 16 = 0.16 \text{ nT}^2$. The value of $\langle B_{\text{T}}^2 \rangle$ should be as small as possible, but since the maps provide only a rough estimate, we set the goal value for S_{Trans} at 0.5 nT^2 . To avoid producing local inhomogeneities due to strong currents in the trim-coils, the tuning is started with a trial value of 2 nT produced per coil on average, resulting in a regularization term S_{Reg} of $(2 \text{ nT})^2 \times 30 = 120 \text{ nT}^2$. Comparing the size of each sum, first guesses for the tuning parameters are $T_{\text{Trans}} = S_{\text{Long}} / S_{\text{Trans}} = 0.32$ and $T_{\text{Reg}} = S_{\text{Long}} / S_{\text{Reg}} = 0.0013$.

Figure 10 shows the minimized values of each sum S_i in Eq. (30) in function of the tuning parameters, with the ranges centered around our initial guesses. The terms are calculated using a typical magnetic field which is measured on-line 30 minutes after degaussing the μ -metal shield, as is the typical procedure during nEDM data

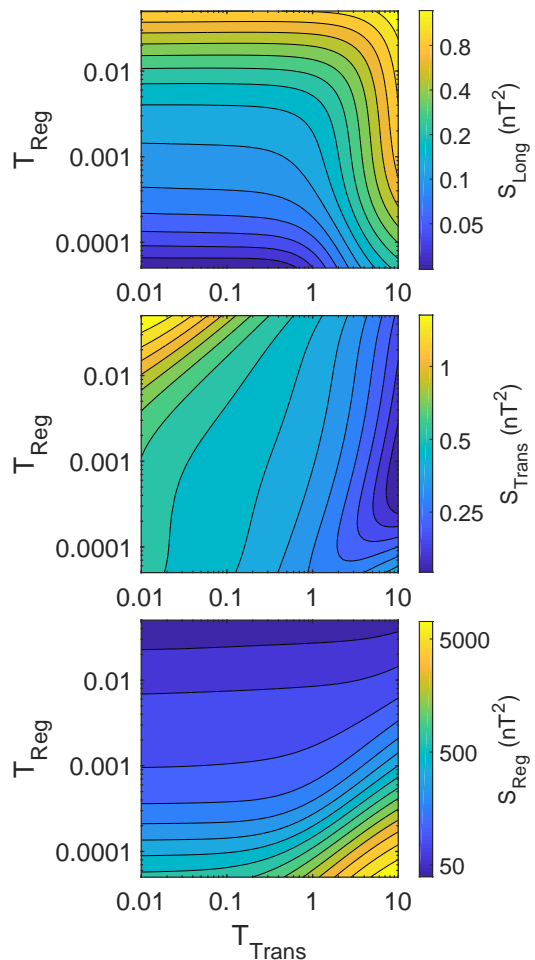


FIG. 10. The behavior of S_{Long} (top), S_{Trans} (middle) and S_{Reg} (bottom) evaluated at the optimal trim-coil currents as a function of the tuning parameters T_{Trans} and T_{Reg} . All scales (including the color scale) are logarithmic.

taking. As is clearly visible in the two uppermost plots of Fig. 10, the tuning parameter T_{Trans} (horizontal axis) determines the relative importance of the longitudinal spread (top) versus the transverse homogeneity (middle). For values of T_{Trans} smaller than 1.0, the longitudinal spread is almost solely determined by the regularization parameter T_{Reg} . The smaller T_{Reg} , the larger the applied currents (bottom), and the smaller the predicted spread of B_z . For T_{Trans} larger than 1, the value of $\langle (B_{\text{T}}^{\text{map}})^2 \rangle$ is significantly reduced at the cost of a worse longitudinal homogeneity and much larger currents. The behavior at large T_{Trans} and small T_{Reg} (bottom right corner of each plot) suggests that it is nearly impossible to have both a small spread in on-line B_z^{CsM} -component and a small $\langle B_{\text{T}}^2 \rangle$ predicted from the maps, even if the restriction on the applied currents is relaxed. This indicates that the estimation of $\langle B_{\text{T}}^2 \rangle$ from the maps is only reliable down to the 0.3 nT^2 level. As the exact size of S_{Trans} is not crucial, T_{Trans} is typically fixed at a value smaller than 1.0 leading to $\langle (B_{\text{T}}^{\text{map}})^2 \rangle$ values smaller than the limit of

TABLE III. Comparison of the transverse neutron spin relaxation time T_2 and the Ramsey contrast α at zero vertical gradient before and after the field homogenization was introduced in 2015. The polarization α_0 at the start of the Ramsey procedure is 0.86 in both datasets. In 2014 the α values were significantly different for the two B_0 field orientations.

Year	B_0 direction	T_2 (s)	α
2014	up	760	0.64
	down	439	0.52
2015 & 2016	up	1620-3000	0.77-0.81
	down	1450-3000	0.76-0.81

2 nT^2 .

The optimal choice for T_{Reg} is not so straightforward. It depends on the initial homogeneity of the magnetic field, as a larger inhomogeneity implies a larger amount of current necessary to compensate. Moreover, as the applied currents become larger, the uncertainty on the measurement of $B_{\text{coil},z}^{\text{CsM}}$ will make the estimation of the longitudinal spread inaccurate and thus reduce the predictive power for the value of α . On top of that, making the magnetic field magnitude the same at all sensor positions does not mean that the field in the storage chamber itself is homogeneous, especially when the applied trim-coil currents are large. For this reason, we typically selected a scan range of 0.0002 to 0.0020 for T_{Reg} and picked out the best setting by measuring the resulting α on-line.

4. Results

Different iterations of the optimization procedure were used during the nEDM data taking period of 2015 and 2016. For each chosen current setting during data taking, the value of $\langle B_T^2 \rangle$ was smaller than 2 nT^2 . The corresponding Ramsey visibilities are shown in Fig. 11. The effect of gravitational depolarization is clearly visible as α decreases when the vertical gradient $\Delta G_{1,0}^S$ moves away from zero. From dedicated measurements at different storage times, we know that the initial polarization α_0 in our storage bottle is 0.86. The α values of 0.76-0.81 at zero gradient then correspond to transverse neutron relaxation times between 1450 s and 3000 s.

The improvement of the neutron spin relaxation time T_2 and the corresponding increase of Ramsey contrast α is summarized in Table III, comparing data from 2014 without CsM based homogenization with data from 2015 and 2016. The transverse relaxation time has more than doubled with the new homogenization procedure, resulting in an increase of α by about 35% and an equal improvement of the nEDM sensitivity. In order to realize the same improvement with neutron statistics, the total number of detected neutrons would have to be increased by a factor of 1.8 due to the \sqrt{N} scaling (see Eq. (1)). This is a significant improvement for an experiment that is scheduled to take data for several years.

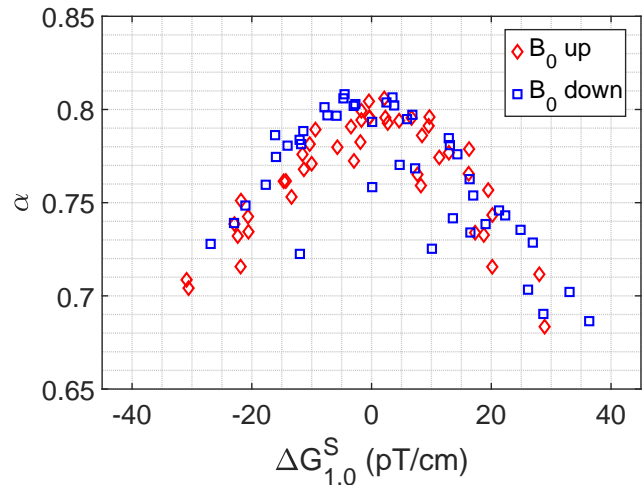


FIG. 11. The Ramsey contrast or visibility α measured during the nEDM data taking period of 2015 and 2016 as a function of the vertical gradient. The ‘zero’ gradient is defined per magnetic field base configuration (or equivalently per set of measurements that are based on the same homogenization result) as the gradient at which the visibility-parabola reaches its highest point. For nonzero vertical gradient, gravitational depolarization reduces the contrast of the Ramsey curve. Note that both B_0 up and B_0 down reach similar visibilities.

V. SUMMARY

We have discussed the design, implementation and performance of the Cs magnetometer array installed at the PSI-nEDM experiment. The compact optical magnetometers are vacuum and HV compatible and are placed on the electrodes above and below the UCN storage chamber, providing on-line gradient information. The sensors are driven by a single diode laser, using beam multiplexing to bring the light to the individual sensors in the vacuum chamber of the experiment. We have explained the phase-feedback mode of sensor operation in the M_x configuration and demonstrated an intrinsic magnetometer sensitivity which is below $50 \text{ fT}/\sqrt{\text{Hz}}$ in the shot noise limit. The final magnetometer noise in the nEDM experiment was significantly larger than the shot noise limit but it did not limit the extraction of important field parameters at the relevant integration time of 180 s. At such large integration times the performance is rather limited by system stability which we could demonstrate to be significantly better than required (see Fig. 9). We have discussed various systematic effects that influence the reading of the magnetometer and estimated an on-line accuracy of 45 to 90 pT. Using a set of two transverse coils, we can run the magnetometers in variometer mode, providing vector information of the local magnetic field.

A model was presented to describe the spatial field distribution, and the precision and accuracy of gradient extraction during nEDM data taking was discussed. Fur-

ther, a magnetic field homogenization procedure, which more than doubled the transverse spin relaxation time of the neutrons, while at the same time keeping magnetic-field-related systematic effects under control, was presented. This resulted in an improvement of 35% of the statistical sensitivity of the nEDM experiment which reduced the time to reach a given statistical sensitivity by a factor of 1.8.

VI. ACKNOWLEDGEMENTS

We would like to thank the mechanical workshop at the University of Fribourg for manufacturing the construction elements of Cs sensors, C. Macchione for the preparation of the paraffin-coated Cs cells and M. Meier and F. Burri for their support during the installation of the Cs magnetometer array and measurements at PSI.

The LPC Caen and the LPSC acknowledge the sup-

port of the French Agence Nationale de la Recherche (ANR) under Reference No. ANR-09-BLAN-0046. P.M. likes to acknowledge support from SNSF-FCS Grant No. 2015.0594 (ETHZ). E.W. acknowledges the fellowship of the Fund for Scientific Research Flanders (FWO). This research was partly financed by the Fund for Scientific Research, Flanders; Grant No. GOA/2010/10 of KU Leuven; the Swiss National Science Foundation projects 126562 (PSI), 140421 (UNIFR), 144473 (PSI), 149211 (ETH), 162574 (ETH), 172626 (PSI), 172639 (ETH), and 181996 (Bern), the Deutsche Forschungsgemeinschaft projects BI 1424/2-1 and /3-1, and Grants No. ST/K001329/1, No. ST/M003426/1, and No. ST/L006472/1 from the Science and Technology Facilities Council (STFC) of the United Kingdom. The original nEDM apparatus without the Cs magnetometer array was funded by grants from the PPARC (now STFC) of the United Kingdom. Our Polish partners wish to acknowledge support from the National Science Centre, Poland, under Grants No. UMO-2015/18/M/ST2/00056 and UMO-2016/23/D/ST2/00715.

-
- [1] E. M. Purcell and N. F. Ramsey, *On the Possibility of Electric Dipole Moments for Elementary Particles and Nuclei*, Phys. Rev. **78**, 807 (1950)
- [2] J. H. Smith, E. M. Purcell and N. F. Ramsey, *Experimental Limit to the Electric Dipole Moment of the Neutron*, Phys. Rev. **108**, 120 (1957)
- [3] G. Bison *et al.*, *Comparison of ultracold neutron sources for fundamental physics measurements*, Phys. Rev. C **95**, 045503 (2017)
- [4] N. F. Ramsey, *A Molecular Beam Resonance Method with Separated Oscillating Fields*, Phys. Rev. **78**, 695 (1950)
- [5] C. Abel *et al.*, *Magnetic-field uniformity in neutron electric-dipole-moment experiments*, Phys. Rev. A **99**, 042112 (2019)
- [6] K. Green *et al.*, *Performance of an atomic mercury magnetometer in the neutron EDM experiment*, Nucl. Inst. Meth. A **404**, 381 (1998)
- [7] C. A. Baker *et al.*, *Apparatus for measurement of the electric dipole moment of the neutron using a cohabiting atomic-mercury magnetometer*, Nucl. Inst. Meth. A **736**, 184 (2014)
- [8] A. Weis and R. Wynands, *Laser-based precision magnetometry in fundamental and applied research*, Optics and Lasers in Engineering **43**, 387 (2005)
- [9] S. Groeger, G. Bison, J.-L. Schenker, R. Wynands and A. Weis, *A high-sensitivity laser-pumped M_x magnetometer*, Eur. Phys. J. D **38**, 239 (2006)
- [10] C. A. Baker *et al.*, *The search for the neutron electric dipole moment at the Paul Scherrer Institute*, Phys. Proc. **17**, 159 (2011)
- [11] K. Bodek *et al.*, *Storage of ultracold neutrons in high resistivity, non-magnetic materials with high Fermi potential*, Nucl. Inst. Meth. A **597**, 222 (2008)
- [12] F. Atchison *et al.*, *Structural characterization of diamond-like carbon films for ultracold neutron applications*, Diamond and Related Materials, **16**, 334 (2007)
- [13] S. Afach *et al.*, *Dynamic stabilization of the magnetic field surrounding the neutron electric dipole moment spectrometer at the Paul Scherrer Institute*, J. Appl. Phys. **116**, 084510 (2014)
- [14] C. Abel *et al.*, *nEDM experiment at PSI: data-taking strategy and sensitivity of the dataset*, EPJ Web Conf. **219**, 02001 (2019).
- [15] P. G. Harris, *The neutron EDM experiment*, arXiv:0709.3100 (2007)
- [16] P. G. Harris *et al.*, *New Experimental Limit on the Electric Dipole Moment of the Neutron*, Phys. Rev. Lett. **82**, 904 (1999)
- [17] C. A. Baker *et al.*, *Improved Experimental Limit on the Electric Dipole Moment of the Neutron*, Phys. Rev. Lett. **97**, 131801 (2006)
- [18] J. M. Pendlebury *et al.*, *Revised experimental upper limit on the electric dipole moment of the neutron*, Phys. Rev. D **92**, 092003 (2015)
- [19] S. Afach *et al.*, *Measurements of a false electric dipole moment signal from ^{199}Hg atoms exposed to an inhomogeneous magnetic field*, Eur. Phys. J. D **69**, 225 (2015)
- [20] S. K. Lamoreaux and R. Golub, *Comment on "Improved Experimental Limit on the Electric Dipole Moment of the Neutron"*, Phys. Rev. Lett. **98**, 149101 (2007)
- [21] A. K. Vershovskii, M. V. Balabas, A. É. Ivanov, V. N. Kulyasov, A. S. Pazgalev and E. B. Aleksandrov, *Fast three-component magnetometer-variometer based on a cesium sensor*, Tech. Phys. **51**, 112 (2006)
- [22] J. M. Pendlebury, *Steps to improve the measurement of the neutron electric dipole moment*, Nucl. Phys. A **546**, 359 (1992)
- [23] N. Castagna, G. Bison, G. Di Domenico, A. Hofer, P. Knowles, C. Macchione, H. Saudan and A. Weis, *A large sample study of spin relaxation and magnetometric sensitivity of paraffin-coated Cs vapor cells*, Appl. Phys. B **96**, 763 (2009)
- [24] E. B. Alexandrov and A. K. Vershovskiy, *M_x and M_z*

- magnetometers, in *Optical Magnetometry* edited by D. Budker and D. F. Jackson Kimball, Cambridge University Press (2013)
- [25] A. Weis, G. Bison and Z. D. Grujić, *Magnetic Resonance Based Magnetometers in High Sensitivity Magnetometers* edited by A. Grosz, M. J. Haji-Sheikh and S. C. Mukhopadhyay, Springer (2017)
- [26] S. Colombo, V. Dolgovskiy, T. Scholtes, Z. D. Grujić, V. Lebedev and A. Weis, *Orientalional dependence of optically detected magnetic resonance signals in laser-driven atomic magnetometers*, Appl. Phys. B. **123**, 35 (2017)
- [27] J. R. Piller, *Accurate optical magnetometry based on precessing spin-aligned atoms*, Master Thesis, University of Fribourg, Fribourg (2016)
- [28] G. Breit and I. I. Rabi, *Measurement of Nuclear Spin*, Phys. Rev. **38**, 2082 (1931)
- [29] F. Bloch and A. Siegert, *Magnetic Resonance for Nonrotating Fields*, Phys. Rev. **57**, 522 (1940)
- [30] J. I. Sudyka, S. Pustelny and W. Gawlik, *Limitations of rotating-wave approximation in magnetic resonance: characterization and elimination of the Bloch-Siegert shift in magneto-optics*, New J. Phys. **21**, 023024 (2019)
- [31] W. Happer and B. S. Mathur, *Effective Operator Formalism in Optical Pumping*, Phys. Rev. **163**, 12 (1967)
- [32] Z. D. Grujić, P. A. Koss, G. Bison and A. Weis, *A sensitive and accurate atomic magnetometer based on free spin precession*, Eur. Phys. J. D **69**, 135 (2015)
- [33] S. Afach *et al.*, *Highly stable atomic vector magnetometer based on free spin precession*, Opt. Express **23**, 22108 (2015)
- [34] E. Wursten, *A new precise measurement of the neutron electric dipole moment*, PhD Thesis, University of Leuven, Leuven (2020)
- [35] F. Grossetête, *Relaxation par collision d'échange de spins*, J. Phys. **25**, 383 (1964); **29**, 456 (1968)
- [36] Y. Shi, T. Scholtes, Z. D. Grujić, V. Lebedev, V. Dolgovskiy and A. Weis, *Quantitative study of optical pumping in the presence of spin-exchange relaxation*, Phys. Rev. A **97**, 013419 (2018)
- [37] S. Appelt, A. Ben-Amar Baranga, C. J. Erickson, M. V. Romalis, A. R. Young and W. Happer, *Theory of spin-exchange optical pumping of ^3He and ^{129}Xe* , Phys. Rev. A **58**, 1412 (1998)
- [38] G. Wyszynsky, *Development of magnetic field control systems in the nEDM experiment*, PhD Thesis, Jagiellonian University, Cracow (2015)
- [39] P. G. Harris, J. M. Pendlebury, and N. E. Devenish, *Gravitationally enhanced depolarization of ultracold neutrons in magnetic-field gradients*, Phys. Rev. D **89**, 016011 (2014)
- [40] S. Afach *et al.*, *Gravitational depolarization of ultracold neutrons: Comparison with data*, Phys. Rev. D **92**, 052008 (2015)